Enhanced catalytic activity by topological flat bands at the charge neutrality point

Yang Song [1,*] Wen-Han Dong [2,3,*] Jie Yang,[1] Ziyuan Liu,[1] Mengxi Liu,[4] Jia Zhu,[1] Shixuan Du,[3]
Feng Liu [5,†] and Lizhi Zhang [1,‡]

[1]*Laboratory of Theoretical and Computational Nanoscience, National Center for Nanoscience and Technology, Beijing 100190, China*
[2]*State Key Laboratory of Low Dimensional Quantum Physics and Department of Physics, Tsinghua University, Beijing 100084, China*
[3]*Beijing National Laboratory for Condensed Matter Physics and Institute of Physics, Chinese Academy of Sciences, Beijing 100190, China*
[4]*Key Laboratory of Standardization and Measurement for Nanotechnology, National Center for Nanoscience and Technology,
Beijing 100190, China*
[5]*Department of Materials Science and Engineering, University of Utah, Salt Lake City, Utah 84112, United States*

The topological flat band (TFB) at the charge neutrality point (CNP) has attracted much recent interest for its physical properties in realizing exotic quantum states, while its implication on materials' chemical properties remains largely unknown. Here, we predict the TFB@CNP in two-dimensional covalent and metal organic frameworks (COFs and MOFs) can enhance catalysis. Using density-functional theory and tight-binding calculations, we show that in a class of COFs and MOFs underlined by a diatomic kagome lattice model, TFB@CNP can be designed by tuning the relative intra- and interkagome lattice hopping in correlation with electron filling. Remarkably, using hydrogen evolution reaction as an example, we illustrate that the catalytic activity of abundant active sites in COFs and MOFs can be significantly enhanced when they are involved in forming the TFB@CNP. Our findings open a promising direction that integrates topological physics with reaction chemistry in the new platform of high-performance TFB-enhanced catalysis.

I. INTRODUCTION

The topological flat band (TFB) represents a unique class of delocalized electronic states beyond the highly localized d or f orbital states [1]. Its extremely narrow bandwidth gives rise to a wide range of intriguing strongly correlated physical phenomena [2–16], such as unconventional superconductivity [9,10] and excitonic Bose-Einstein condensation [16]. However, the implication of TFB on materials' chemical properties remains largely unexplored. In this work, we predict that the presence of TFB at the charge neutrality point (CNP) can significantly enhance a material's existing catalytic activity. The TFB@CNP contributes an extremely high electron density of states (DOS) around the Fermi level to facilitate the charge transfer process for chemical adsorption, which bears some similarity with high DOS of localized d orbitals, but the physical origin and working principle of TFB catalysis have some notable differences from the d-band catalysis [17]. The TFB is formed by destructive interference coded in the lattice and/or orbital symmetry of the whole crystal lattice [1,18] rather than the localized atomic orbitals. Therefore, it may not offer a specific catalytic site, but instead enhance the activity of existing catalytic sites that are involved in forming the TFB. In particular, the TFB may act as an electron reservoir during chemical reaction, changing electron occupation with a nearly

fixed Fermi level, while a d-band center will shift position with different electron filling.

Recently, the topological electronic states have been proposed for catalysis [19–22], but the field of topological catalysis is still in its infancy. We note that physically the topological surface state (TSS) originates from bulk Bloch wave functions terminated at the surface via bulk-boundary correspondence. Thus the TSS is robust against surface adsorption adding an "impurity." Conversely, surface adsorption might not react catalytically with a TSS as it does with a trivial local d-orbital state in surface, but only modify slightly the TSS distribution in and around bulk band gap [23,24]. Also, the TSS typically consists of Dirac bands with a vanishing DOS at the Fermi level, unfavorable for catalysis. In these regards, our proposed TFB-enhanced catalysis differs significantly from the previously proposed topological catalysis based on the TSS [19–22].

In general, there are two categories of TFBs. One we call the unit-cell TFB [25,26], hosted in crystalline lattices with a few atoms per unit cell [27–29] and formed by destructive interference with an arbitrary value of nearest-neighbor (NN) hopping t [30]. The other one is the supercell TFB [8], formed by flattened Dirac bands with reduced hopping t and tuned interlayer interaction [31]. As an advantage, the supercell TFBs naturally exist at the CNP to be easily accessible, while the unit-cell TFBs are usually far away from the Fermi level. Partly for this reason, interesting properties of the supercell TFBs have been widely shown recently, including an enhancement of electrochemical reaction in the twisted bilayer graphene (TBG) [32], while experimental demonstration of

---

*These authors contributed equally to this work.
†Contact author: ftiger.liu@utah.edu
‡Contact author: zhanglz@nanoctr.cn

the unit-cell TFBs [33] and their properties remains largely elusive. However, of interest here, the unit-cell TFB materials can have some advantages; e.g., they can possess much higher density of catalytic sites than the supercell ones, whose active sites exist only at the AA stacking regions in a very large moiré pattern (e.g., $\sim$170 nm^2 for the 1.1° TBG).

Covalent and metal organic frameworks (COFs and MOFs) have already been widely used as catalysts due to their large accessible area (porous structure), abundant active sites [34,35], and potentially high carrier mobilities [36–38]. Also, COFs and MOFs are well-known unit-cell materials to host TFBs because of their diverse sublattice symmetries [5,29,39–53], such as the well-known kagome lattices [5,45,46]. It is desirable to achieve the TFB@CNP because the conductive COFs and MOFs are usually endowed with a better catalytic activity [54,55]. But, as mentioned above, the unit-cell TFBs are usually located far away from the Fermi level, with only a few exceptions [13,56]. Therefore, a prerequisite condition is to design and discover the TFB@CNP in two-dimensional (2D) organic frameworks.

Here, we propose an effective approach to realize TFB@CNP focusing COFs and MOFs with an underlying diatomic kagome lattice (DKL). Based on density-functional theory (DFT) and tight-binding (TB) calculations, we predict that both a family of 2D COFs (3R-*X*, *X* = F, Cl, Br; 3R = aza[3]radialene) and MOFs (HAT-Sn; HAT = 1,4,5,8,9,12-hexaazatriphenylene) can host the TFB@CNP to further enhance the catalytic activity of their active sites that are involved in TFB formation. The prototypes of these COFs and MOFs have already been experimentally synthesized [57,58]. We show that in both families, TFBs can be designed exactly at the CNP by tuning the relative strength of intra- and interkagome lattice hopping in correlation with electron filling. Remarkably, by calculating the free energy diagram of the hydrogen evolution reaction (HER), we show that 3R-*X* (*X* = F, Cl, Br) and HAT-Sn possess significantly improved HER activity in the presence of TFB@CNP.

II. COMPUTATION METHODS

DFT calculations were performed in the Vienna *ab initio* simulation package (VASP) [59,60] adopting the projector-augmented wave (PAW) method and the Perdew-Burke-Ernzerhof (PBE) [61] functional. The Grimme-D3 method [62] was used to describe the van der Waals interaction between 3R-Cl COF layer and the metal substrate [63]. Ag (111) substrates were modeled by three layered slabs with two bottom layers fixed and the top layer relaxed. The vacuum layers for all structural models were larger than 15 Å. The atoms were fully relaxed until the force on each atom was less than 0.01 eV Å^{-1} in the monolayer COF or MOF systems and less than 0.02 eV Å^{-1} in the COF/Ag(111) systems. The energy cutoff of the plane-wave basis was set at 600 eV. The Brillouin zone was sampled by a Gamma-centered k mesh [64] of 3×3×1. The lattice constants of 3R-*X* (*X* = H, F, Cl, Br) are 15.12, 15.11, 15.13, and 15.11 Å, respectively. The lattice constants of HAT-Sn and HAT-Pb are 15.39 and 15.60 Å, respectively. The *ab initio* molecular dynamics (AIMD) simulations were performed under

the canonical (*NVT*) ensemble. The scalar relativistic effect was considered in the PAW pseudopotential for all calculations. The fully relativistic effect (i.e., spin-orbit coupling) was checked to have a negligible influence on the Gibbs free energies. Therefore, these extra calculation results are not included.

The standard hydrogen electrode (SHE) model was used for the proton-electron transfer steps of the HER process [65], in which the applied electric potential is 0 V, pH is 0, temperature is 298.15 K, and the pressure of H$_2$ is 1 bar. Under these standard conditions, the hydrogen evolution is at equilibrium: $H^+ + e^- \leftrightarrow \frac{1}{2}H_2$.

Since the active sites of the studied COFs and MOFs are spatially separated from each other, we adopted the Volmer-Heyrovský mechanism for HER [66]. In the first step, a Volmer reaction, the hydrogen cation (H$^+$, i.e., proton) from the solution adsorbs on the COF or MOF surface at the chemically active sites, and transforms into H*, $H^+ + e^- + ^* \rightarrow H^*$, where $*$ denotes the active site that binds with H. In the second step, a Heyrovský reaction, another H$^+$ comes by the adsorbed H atom (H*), pulling away from the surface and releasing as H$_2$, $H^+ + e^- + H^* \rightarrow H_2$.

The change of Gibbs free energy (ΔG_{H^*}) for the Volmer reaction is generally calculated using gas-phase approximation as [65]

$$\Delta G_{H^*} \approx \Delta E_H + \Delta E_{ZPE} - T \Delta S_H. \tag{1}$$

Note that the thermal correction derived from the integral of heat capacity is not included in Eq. (1), owing to its minimal contribution at room temperature. Here, ΔE_H is the adsorption energy of hydrogen on the substrate. It can be obtained by the following formula:

$$\Delta E_H = \frac{1}{n}\left[E(H^*) - E(^*) - \frac{n}{2}E(H_2) \right], \tag{2}$$

where $E(H^*)$, $E(^*)$, and $E(H_2)$ are the total energies of the adsorption system, the 2D COFs and MOFs, and the hydrogen molecule, respectively. n is the number of hydrogen atoms. ΔE_{ZPE} is the difference of the zero-point energy (ZPE) of the system between adsorbed and gaseous hydrogen, which can be obtained by the following formula:

$$\Delta E_{ZPE} = \frac{1}{n}\left[E_{ZPE}(H^*) - E_{ZPE}(^*) - \frac{n}{2}E_{ZPE}(H_2) \right], \tag{3}$$

where $E_{ZPE}(H^*)$, $E_{ZPE}(^*)$, and $E_{ZPE}(H_2)$ are the ZPE values of the adsorption system, the 2D COFs and MOFs, and the hydrogen molecule, respectively. n is the number of hydrogen atoms.

In particular, the contributions of all atoms were taken into account in the ZPE calculations that

$$E_{ZPE} = \Sigma_i^{3N} \frac{h\nu_i}{2}, \tag{4}$$

where h is the Planck constant, ν_i is the vibrational frequency of harmonic phonons calculated by the finite displacement method, and N is the total number of atoms in a system. The temperature T is set to 298.15 K. ΔS_H is the corresponding entropy change, as given by

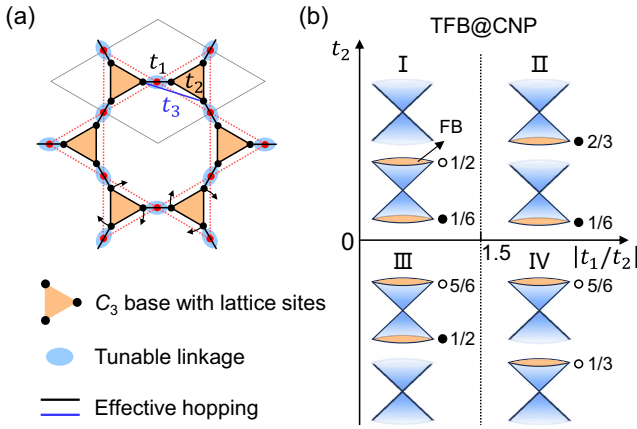$$\Delta S_H = -\frac{1}{2}S^0_{H_2}, \tag{5}$$

FIG. 1. Designing TFB@CNP in DKL using COFs and MOFs. (a) Schematics of DKL. Red dots are kagome lattice sites; black dots are DKL sites. The orange triangles and blue ovals denote C_3 bases and linkages which constitute COFs and MOFs. The arrows indicate rotation of diatomic dumbbell or equivalently rotation of triangle bases. The first NN inter- and intrakagome hopping are t_1 and t_2, respectively. The second NN interkagome hopping is t_3. (b) Phase diagram of DKL under different hopping conditions. Four regions are divided according to the band structures. The blue hourglasses with orange bottoms denote Dirac bands and connected FBs. The solid (open) dots denote the electronlike (holelike) TFB@CNP under corresponding filling factors.

Considering the small vibrational entropy of adsorbed hydrogen, $S_{H_2}^0$, the entropy of hydrogen under standard conditions is 130.680 J/(K mol), so that $T \Delta S_H \approx 0.202$ eV. The calculation results of ΔE_H and ΔE_{ZPE} are summaried in Table I.

III. RESULTS AND DISCUSSION

A. Theoretical design of TFB@CNP

We first discuss an inverse design process of 2D lattices with TFB@CNP based on a TB lattice Hamiltonian in correlation with electron band filling in the DKL model, as illustrated in Fig. 1(a). The red dots and dashed lines represent the kagome lattice. One can split each kagome lattice site (red dot) symmetrically into two atoms (black dots), like a

diatomic dumbbell connected by solid lines, to form a DKL, with two subkagome lattices. Let t_1 and t_3 represent the first and second NN interkagome lattice hopping, respectively, and t_2 the intrakagome hopping [Fig. 1(a)]. It has been shown that [51] at the chiral limit, the DKL is equivalent to a bipartite double cover of a line graph in graph theorem by setting $t_2 = 0$; then chiral symmetry leads to the formation of two sets of kagome bands of opposite chirality, each having a FB sitting above or below two Dirac bands. Importantly, the chiral symmetry guarantees the two TFBs (so-called yin-yang flat bands) to be at or around the CNP [52]. However, in most real materials, chiral symmetry is broken because $t_2 \neq 0$. Therefore, our focus here is to find conditions to have one TFB@CNP for achiral DKL models.

A very rich phase diagram of TB band structures of DKL has been previously mapped out in the parameter spaces of t_1, t_2, and t_3 [53]. Since we are interested in COFs and MOFs with very large ligand groups, t_3 at a large distance can be neglected. Then the six-band TB Hamiltonian of a DKL is written as

$$H = t_1 \sum_{\langle i,j \rangle} c_i^\dagger c_j + t_2 \sum_{\langle\langle i,j \rangle\rangle} c_i^\dagger c_j + \varepsilon \sum_i c_i^\dagger c_i, \quad (6)$$

where $c_i^\dagger$ (c_i) is the creation (annihilation) operator at lattice site i and ε is the on-site energy. As illustrated in Fig. 1(b), there are four typical types of achiral DKL band structures, I, II, III, and IV, depending on the ratio of $|t_1/t_2|$ and the sign of t_2. All four types host two TFBs located at different energies, and the electron filling required to achieve TFB@CNP can be easily determined [see Fig. 1(b)].

Interestingly, the band structures remain the same if one rotates the diatomic dumbbell about the kagome lattice sites [see black arrows in Fig. 1(a)], as the rotated DKL Hamiltonian is a unitary transformation of the original one [46] [see Fig. 2]. This gives extra flexibility in material realization of TFB@CNP, as shown below. We choose the case that t_1, $t_2 > 0$ as an example to explain the underlying reason for the equivalence of the DKL under the C_{3z}-symmetric rotations. We begin with the TB model of DKL. One can consider the following 6×6 Hamiltonian as the matrix representation for Eq. (6), where $\vec{v}_m$ ($m = 1, 2, 3, 4, 5, 6$) are nearest position vectors, as depicted in Fig. 2(a). There are two sets of triangles in a DKL, forming a compound lattice.

$$H^{DKL}(\vec{k}) = \begin{bmatrix} 0 & t_1 e^{i\vec{k}\cdot\vec{v}_5} & t_1 e^{i\vec{k}\cdot\vec{v}_4} & t_2 e^{i\vec{k}\cdot\vec{v}_1} & 0 & 0 \\ t_1 e^{-i\vec{k}\cdot\vec{v}_5} & 0 & t_1 e^{i\vec{k}\cdot\vec{v}_6} & 0 & t_2 e^{i\vec{k}\cdot\vec{v}_2} & 0 \\ t_1 e^{-i\vec{k}\cdot\vec{v}_4} & t_1 e^{-i\vec{k}\cdot\vec{v}_5} & 0 & 0 & 0 & t_2 e^{i\vec{k}\cdot\vec{v}_3} \\ t_2 e^{-i\vec{k}\cdot\vec{v}_1} & 0 & 0 & 0 & t_1 e^{-i\vec{k}\cdot\vec{v}_4} & t_1 e^{-i\vec{k}\cdot\vec{v}_5} \\ 0 & t_2 e^{-i\vec{k}\cdot\vec{v}_2} & 0 & t_1 e^{i\vec{k}\cdot\vec{v}_4} & 0 & t_1 e^{i\vec{k}\cdot\vec{v}_6} \\ 0 & 0 & t_2 e^{-i\vec{k}\cdot\vec{v}_3} & t_1 e^{i\vec{k}\cdot\vec{v}_5} & t_1 e^{-i\vec{k}\cdot\vec{v}_6} & 0 \end{bmatrix}. \quad (7)$$

By solving the Hamiltonian in Eq. (7) with $t_1/t_2 = 1.8$ and the on-site energy $\varepsilon = -0.8$ eV, we obtain the band structure shown in Fig. 2(d). We find the varying of t_1/t_2 can lead to

$2 + 4$ to $3 + 3$ band transitions, which are summarized in Fig. 1(b). Such a transition means the TFBs in DKL are highly tunable, which offers more chances for achieving TFB@CNP
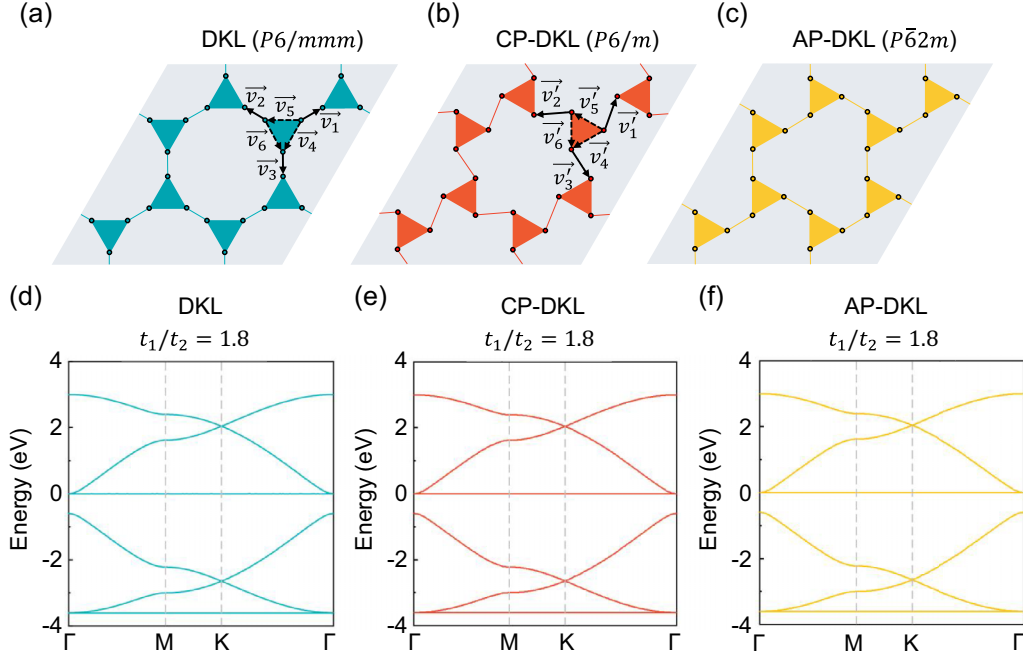
FIG. 2. Equivalence of the DKL under the C_{3z}-symmetric rotations. (a)–(c) Schematics of the (normal) DKL, cophase (CP), and antiphase (AP) rotated DKLs, respectively. (d)–(f) Band structures of the tight-binding Hamiltonian with $t_1/t_2 = 1.8$ for DKL, CP DKL, and AP DKL, respectively. The on-site energy ε is set to -0.8 eV.

than the "simple" lattices, such as kagome lattice. Notice there is also a degree of freedom to rotate the triangles in kagomelike structures. The known example is the rotation transformation from a kagome lattice to a CT lattice [47]. We have demonstrated such a transformation in superatomic zirconium dichlorides [67]. To be more general, we consider the possible triangle rotations in DKLs. As shown in Figs. 2(b) and 2(c), there are two ways to rotate the two triangles, i.e., cophase (CP) rotation and antiphase (AP) rotation. Here, we mainly focus on the CP DKL, and a similar conclusion can be drawn for the AP DKL. For the CP DKL, up to the nearest hopping, $H^{\mathrm{CP}}(\vec{k})$ takes a similar form as $H^{\mathrm{DKL}}(\vec{k})$, while the only difference is to replace $\vec{v_m}$ with $\vec{v'_m}$ ($m = 1, 2, 3, 4, 5, 6$). We prove that $H^{\mathrm{DKL}}(\vec{k})$ can convert into $H^{\mathrm{CP}}(\vec{k})$ by a unitary transformation $UU^{\dagger} = I$, i.e., $H^{\mathrm{CP}}(\vec{k}) = UH^{\mathrm{DKL}}(\vec{k})U^{-1}$, and U takes the form

$$U = \mathrm{diag}[1,\ e^{i\vec{k}\cdot(\vec{v_5}-\vec{v'_5})},\ e^{i\vec{k}\cdot(\vec{v_4}-\vec{v'_4})},\ e^{i\vec{k}\cdot(\vec{v_1}-\vec{v'_1})},\ e^{i\vec{k}\cdot(\vec{v_2}+\vec{v_5}-\vec{v'_2}-\vec{v'_5})},$$

$$e^{i\vec{k}\cdot(\vec{v_3}+\vec{v_4}-\vec{v'_3}-\vec{v'_4})}]. \qquad (8)$$

It means that the rotation is equal to a unitary transformation between $H^{\mathrm{CP}}(\vec{k})$ and $H^{\mathrm{DKL}}(\vec{k})$, so that $H^{\mathrm{CP}}(\vec{k})$ and $H^{\mathrm{DKL}}(\vec{k})$ share the same band eigenvalues, as shown in Figs. 2(d) and 2(e). For the AP DKL, we also obtained the same band eigenvalues [see Fig. 2(f)]. In this sense, the CP DKL (AP DKL) is equivalent to the pristine one.

B. Material prediction of TFB@CNP

We next predict materials with TFB@CNP in 2D COFs and MOFs underlined by the DKL model. Based on the above analyses, one may approach this in two ways. For given electron filling, one can tune the ratio of t_1/t_2 by changing the ligand groups and/or linkage atoms between the groups. For example, at 2/3 filling, if one increases the $t_1/t_2 > 3/2$, a TFB@CNP can be created when the band structure changes from type I to type II, as shown in the top panel of Fig. 1(b). Alternatively, for a given type of band structure, one tunes the electron filling; for example, the required electron filling for type I is 1/6 or 1/2 to have a TFB@CNP. Here we adopt the first approach, because, on one hand, the tunable linkages are easier to implement in experiments; on the other hand, a direct comparison between the catalytic behaviors of a TFB at and not at CNP can be made to highlight the importance of TFB@CNP for enhancing catalysis.

We first show DFT calculations for COFs with TFB@CNP. As depicted in Fig. 3(a), the 3R-*X* (X = F, Cl, Br) family has the benzene halides of C_2 symmetry sitting at the kagome sites, which are linked by aza[3]radialene (3R) of C_3 symmetry, forming a CP DKL with a $P6/m$ symmetry and a small counterclockwise rotation of two organic groups [see Fig. 2(b)]. The prototype 3R-Cl COF has recently been synthesized via $[1 + 1 + 1]$ cycloaddition of the precursor on silver surface [57], and our simulated STM image agrees well with the experimental STM images [Fig. 4]. We also confirm the dynamical and thermodynamic stability of 3R-*X* COFs (see Figs. S1 and S2 in the Supplemental Material (SM) [68]).

Figure 3(b) shows the DFT band structure of 3R-Cl, with one FB located exactly at the CNP. Using the irreducible representations of this FB, parity eigenvalues of $+1$ (Γ point) and -1 (M points) are revealed, indicating a nontrivial $\mathbb{Z}_2 = 1$ band topology [69]. The charge density of this TFB is found to be distributed over the whole lattice including both N and
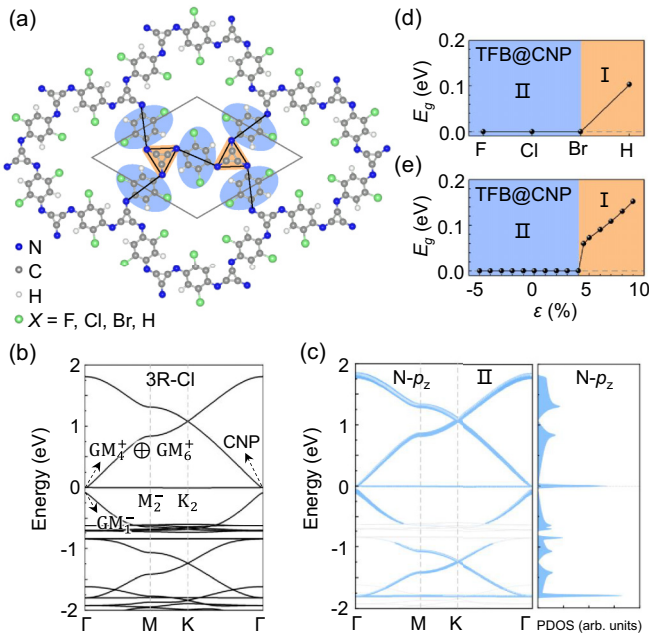
FIG. 3. TFBs in the 3R-X (X = F, Cl, Br, H) COFs. (a) Structure of the 3R-X COFs with a rotated DKL (black lines). Here, the 3R groups serve as the C_3 bases (shaded in orange), while the benzene halides are tunable linkages (shaded in blue). (b) Band structure of 3R-Cl. The irreducible representations of high-symmetry points are labeled, where the sign of superscript denotes parity. (c) Projected bands and PDOS for the p_z orbitals of N atoms. (d) Band gaps of 3R-X COFs. (e) Band gaps of 3R-Cl under biaxial strain (ε). The positive (negative) ε corresponds to tensile (compressive) strain.

C atoms (see SM Fig. S3(a) [68]), consistent with previous works [27]. The projected bands and projected DOS (PDOS) in Fig. 3(c) and SM Fig. S4 [68] confirm that electronic states near the Fermi level can be captured by a simple, effective six-band DKL model, having effective lattice sites near N atoms [see Fig. 3(a)]. By electron counting, we reveal the 3R-Cl COF has 2/3 filled DKL bands, corresponding to case II in Fig. 1(b). Furthermore, one may apply the common strategy of element substitution and strain engineering [29,41] to tune the hopping ratio of t_1/t_2. We found that 3R-X (X = F, Cl, Br) have type II DKL bands with exactly TFB@CNP, while 3R-H is a semiconductor of the type I bands [see Fig. 3(d)].
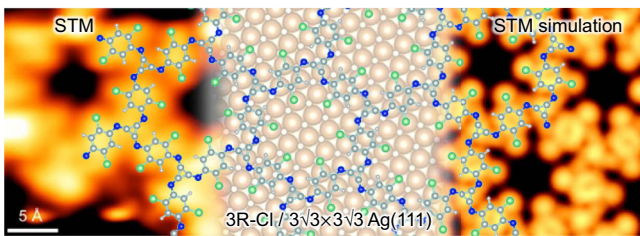

FIG. 4. 3R-Cl synthesis on Ag(111) substrate. Merged image for the experimental STM image, atomic structure, and simulated STM image of 3R-Cl on Ag(111) substrate. The STM image is adapted from Ref. [57]. The energy range of the STM simulation is from -1 eV to the Fermi level (0 eV). The unit cell is 1×1 3R-Cl on $3\sqrt{3}\times3\sqrt{3}$ Ag(111).

Since the electronegativities of the halogen atoms are stronger than that of the hydrogen atoms, the benzene halides are more likely to attract the lone pair electrons of N atoms than benzenes, so that 3R-X (X = F, Cl, Br) have a larger t_1/t_2 ratio than 3R-H. This is supported by the significant different TFB charge distribution of 3R-Cl from that of 3R-H (see SM Fig. S3 [68]). Thus, by modifying the linkages with element substitution, a transition of DKL bands is achieved in 3R-X COFs. Applying biaxial strain shows another way of tuning t_1/t_2 through mostly bond rotation. In Fig. 3(e), one can see the transition of DKL bands of 3R-Cl from type II to type I, which occurs under a tensile strain larger than 4%.

We next predict the MOF with TFB@CNP. We consider the HAT-M (M = Sn, Pb) MOFs, whose prototypes have been recently synthesized by on-surface reaction [58]. As shown in Fig. 5(a), the metal atom sitting on the kagome site acts as a linkage to bond HAT molecules having C_3 symmetry, forming a pristine DKL without rotation [see Fig. 2(a)]. The band structure of HAT-Sn corresponds to type III at 1/2 filling [Fig. 1(b)], featured with the TFB@CNP [Fig. 5(b)]. The projected band structure and PDOS of HAT-Sn show that the six bands near the Fermi level are contributed by p_z orbitals of both Sn atoms and HAT molecules [Fig. 5(c)]. In particular, the TFB at the Fermi level is composed of p_z orbitals of Sn, C, and N atoms, which will participate in the (quick) charge transfer process of HER. Thus, the charge density from the TFB@CNP is globally distributed on the whole framework [Fig. 5(d)]. These features agree well with a DKL model, whose effective sites are shown by the black dots. The black circles approximately mark the charges contributing the effective sites. Differently, HAT-Pb has type IV DKL bands [Fig. 5(e)]. A DKL band transition from type III to type IV is induced by changing the linkage metal atom. For HAT-Pb, the larger Pb atom increases the distance between HAT molecules, leading to a smaller $|t_2|$ compared with HAT-Sn. We also confirm the thermodynamic stability of HAT-M MOFs on a suitable substrate at low temperature (see SM Fig. S5 [68]).

C. Catalytic enhancement by TFB@CNP

Given the material realization of TFB@CNP, we next explore the catalytic activity of both COFs and MOFs, using HER as an example. For HER, it has been shown that the experimentally measured exchange current in solution can be correlated with the calculated H adsorption free energy (ΔG_{H^*}) in the gas phase, which follows a volcano-shaped curve with the peak positions corresponding to the highest activity [65]. In general, the peak position of the highest activity corresponds with $\Delta G_{H^*} \approx 0$ eV. Therefore, the catalyst with the smallest $|\Delta G_{H^*}|$ exhibits the highest activity, which indicates an optimal hydrogen adsorption strength—neither too weak for effective H binding nor too strong for rapid H_2 release [70]. For example, Fig. 6(a) shows the two-step Volmer-Heyrovský mechanism of the HER process [66]. In the first step of a Volmer reaction, the hydrogen cation (H^+, i.e., proton) from solution adsorbs on the 3R-X (X = F, Cl, Br) COF surface at the chemically active sites, which are N atomic sites, and transforms into H^*, $H^+ + e^- + * \rightarrow H^*$, where * denotes the active N site that binds with H. In the
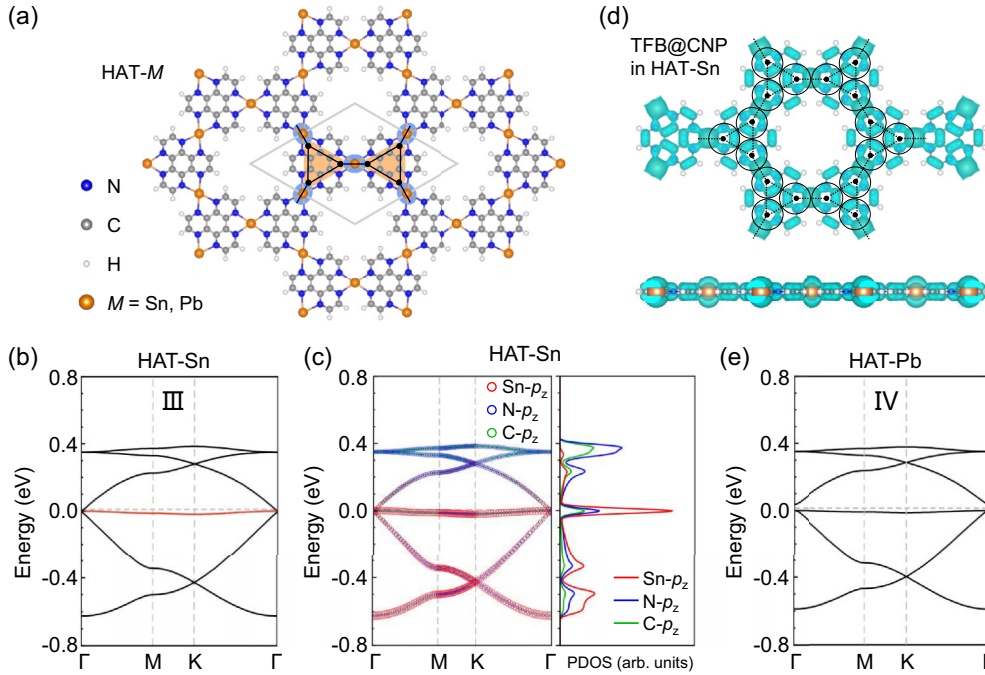
FIG. 5. TFBs in the HAT-*M* (*M* = Sn, Pb) MOFs. (a) Structure of the HAT-*M* with a DKL. The black lines outline a DKL. The orange labeled HAT molecules are C_3 bases, whose effective sites locate at the black dots. The blue-shaded metal atoms are tunable linkages. (b) Band structures of HAT-Sn. The red line highlights the TFB@CNP. (c) Projected bands and PDOS of HAT-Sn. (d) Global charge density distribution of the TFB@CNP of HAT-Sn. (e) Band structures of HAT-Pb.

second step of a Heyrovský reaction, another H^+ comes by the adsorbed H atoms (H^*), pulling away from the surface and releasing as H_2, i.e., $H^+ + e^- + H^* \rightarrow H_2$. Therefore, for simplicity, we have calculated the change of Gibbs free energy ΔG_{H^*} of the first step in the gas phase, as one key indicator for HER activity. We found that ΔG_{H^*} is $\sim 0.06-0.12$ eV when the H^* coverage (μ) is 1.0 for 3R-*X* (*X* = F, Cl, Br) [see Fig. 6(b)], which is comparable with the activity of Pt (0.08 eV) [71] and Os$-N_3S_1$ (0.09 eV) [72], as well as other topological catalysts, such as TiB_2 (0.08 eV) [19], TiSi (0.04 eV) [20], PtGa (0.131 eV) [21], and H4CdPc-COF(F) (−0.016 eV) [73]. The rather low absolute value of ΔG_{H^*} (<0.1 eV) indicates high catalytic efficiency for HER. The detailed computational methods of ΔG_{H^*} can be found in the Computation Methods section. ΔG_{H^*} for different μ are evaluated and listed in Table I. When μ is 1.0, the absolute value of ΔG_{H^*} is optimal for HER.

Therefore, the combination of abundant active N sites with TFB@CNP in 3R-*X* (*X* = F, Cl, Br) COFs makes them promising for high-performance catalysis. We also test the HER catalytic activity of 3R-Cl on Ag(111) surface (SM Fig. S6 [68]), whose ΔG_{H^*} is −0.003 eV, indicating still an excellent HER performance. Similarly, TFB@CNP in HAT-Sn MOF is found effective for catalyzing HER. Here Sn atoms are found to be active sites for H^* in adsorption in HAT-Sn [Fig. 6(c)]. When the H^* coverage $\mu = 0.33$, the optimal ΔG_{H^*} is 0.08 eV.

D. Comparative studies to confirm the role of TFB@CNP

To verify the role of TFB@CNP in the enhanced catalysis, we perform computational experiments by moving the

TFB away from the CNP, using atom substitution or strain engineering. Specifically, we have calculated the ΔG_{H^*} for HER in the semiconducting cases without TFB@CNP, e.g., the 3R-H COF [Fig. 3(d)], the strained 3R-Cl COF [Fig. 3(e)], and the HAT-Pb MOF [Fig. 5(e)]. The calculated ΔG_{H^*} for 3R-H is 0.23 eV [marked by the black line in Fig. 6(b)], significantly larger than that for 3R-Cl (0.07 eV), while the ΔG_{H^*} for 3R-Cl under biaxial strain is 0.09 eV for $\varepsilon= 5\%$ and 0.15 eV for $\varepsilon= 10\%$, respectively, which are noticeably

TABLE I. Parameters used in the calculations of the change of Gibbs free energies (ΔG_{H^*}). Hydrogen adsorption energies ΔE_H, the difference of the zero-point energy between adsorbed and gaseous hydrogen ΔE_{ZPE}, and ΔG_{H^*} with different H^* coverages μ.

| Systems	ΔE_H (eV)	ΔE_{ZPE} (eV)	ΔG_{H^*} (eV)
3R-Cl ($\mu = 0.17$)	−1.194	0.199	−0.79
3R-Cl ($\mu = 0.33$)	−1.155	0.191	−0.76
3R-Cl ($\mu = 0.50$)	−1.005	0.189	−0.61
3R-Cl ($\mu = 0.67$)	−0.957	0.181	−0.57
3R-Cl ($\mu = 0.83$)	−0.549	0.164	−0.18
3R-Cl ($\mu = 1.00$)	−0.285	0.154	0.07
3R-Cl ($\mu = 1.00$) (strain: 5%)	−0.282	0.173	0.09
3R-Cl ($\mu = 1.00$) (strain: 10%)	−0.246	0.190	0.15
3R-F ($\mu = 1.00$)	−0.236	0.153	0.12
3R-Br ($\mu = 1.00$)	−0.294	0.150	0.06
3R-H ($\mu = 1.00$)	−0.123	0.151	0.23
Sn-HAT ($\mu = 0.33$)	−0.190	0.069	0.08
Sn-HAT ($\mu = 0.67$)	−0.118	0.063	0.15
Sn-HAT ($\mu = 1.00$)	−0.076	0.057	0.18
Pb-HAT ($\mu = 0.33$)	0.091	0.040	0.33
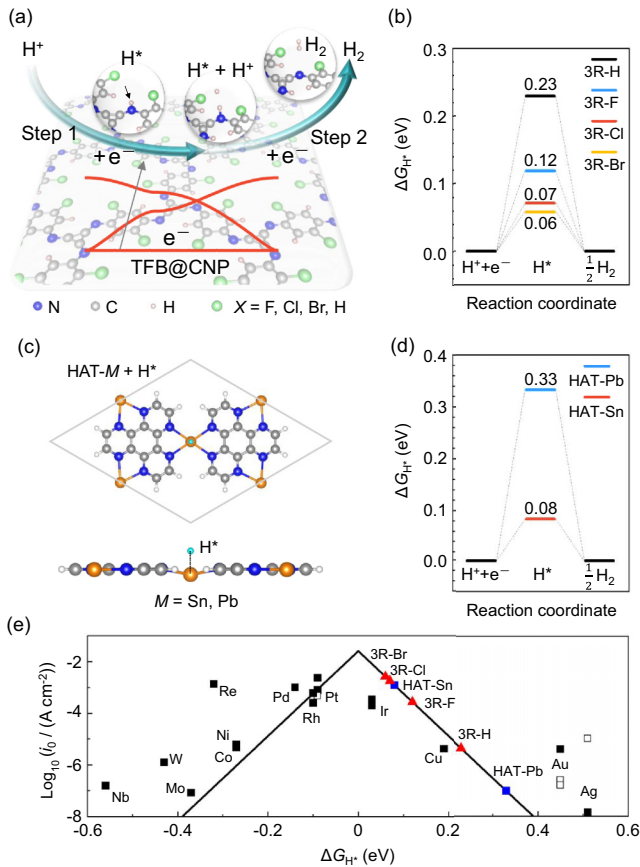
FIG. 6. HER activity of 3R-*X* COFs and HAT-*M* MOFs. (a) Schematic of the HER process of 3R-*X*, in which the N atoms are active sites. (b) The calculated free energy diagrams of HER for 3R-*X* with H* coverage $\mu = 1$. (c) Top and side views of the hydrogen adsorption on HAT-*M*. (d) Calculated free energy diagram of HER for HAT-*M* with H* coverage $\mu = 0.33$. (e) Volcano plot of $\log_{10}(i_0)$ vs calculated hydrogen adsorption free energy (ΔG_{H^*}) for HER catalysts. The $\log_{10}(i_0)$ data of the metal surfaces (black squares) are from experiments [65], while those of the COFs and MOFs (colorful shapes) are given by the volcano curve.

increased over the intrinsic 3R-Cl. Similarly for MOFs, ΔG_{H^*} for the semiconducting HAT-Pb is 0.33 eV [see Fig. 6(d) and Table I], much larger than that of HAT-Sn. These comparisons evidently confirm the significant role of TFB@CNP in enhancing the HER activity.

Furthermore, we compared the catalytic activity of our COF and MOF candidates hosting TFB@CNP with some known high-performance catalysts, such as Pt. In experiments, a catalyst for HER is usually measured by the exchange current density, i_0. Interestingly, the experimentally measured exchange current i_0 has been examined as a function of the theoretically calculated H adsorption free energy (ΔG_{H^*}), which follows a volcano-shaped curve with the peak position occupied metal Pt as the best catalyst [70]. Similarly, we have added a plot of the volcano curve to compare the relative catalytic activities of our COFs and MOFs with previous catalysts in Fig. 6(e). The measured exchange currents (i_0) of the plot are adapted from Table I in Ref. [65], which summarizes the data from the original Refs. [74–79]. Remarkably, both 3R-*X* ($X = $ F, Cl, Br) and HAT-Sn locate near the top

of the volcano curve, indicating their high catalytic activity, comparable with noble metals, such as Pt. In contrast, 3R-H and HAT-Pb, without TFB@CNP, locate near the bottom of the volcano curve.

We note that COFs and MOFs are well known to have abundant catalytically active sites due to reaction chemistry, regardless of TFB. On the other hand, the TFB is formed by the lattice symmetry of all lattice sites, which may or may not be catalytically active. For example, in 3R-*X* COFs, due to atomic rotation, the effective DKL lattice sites are between N and C_1 atoms [Fig. 3(a)], and C_1 contributes more to TFB density than N (see SM Fig. S4 [68]). But only N are active because H are attracted to their lone pair electrons, as shown from the calculated DOS with H adsorbed on N (see Fig. S7(a) [68]), in comparison with H adsorbed on C_1 (see Fig. S7(b) [68]). In HAT-*M* MOFs, metal atoms are active because of strong *M*-H bond formation. Interestingly, what we have shown is that if the active sites, e.g., N in 3R-*X* COFs and *M* in HAT-*M* MOFs, are involved in forming the TFB, then the TFB@CNP can make them even more active. This is because the TFB@CNP contributes large DOS near the Fermi level [see Figs. 3(c) and 5(c)], which enhances not only the adsorption of the adsorbates on the active sites, but also the charge transfer rate during reactions [17]. Finally, in comparison with previous 2D COF and MOF catalysts, such as C_3N_4@graphene [80], our proposed COFs and MOFs, e.g., 3R-Cl, exhibit intrinsic high HER activity, requiring no external interface engineering.

IV. CONCLUSIONS

Taking DKL as a model system, we propose a generic design strategy for realizing TFB@CNP in 2D organic frameworks. Based on DFT and TB calculations, we predict that the TFBs in 3R-*X* COFs and HAT-*M* MOFs, underlined by the DKL, can be tuned by varying linkages or applying biaxial strain. We show that the TFB@CNP can further enhance the HER activity on the abundant active sites in COFs and MOFs. Our findings open a promising direction for high-performance catalysis, and offer a broad prospective for discovering and engineering TFB@CNP in organic frameworks for chemical applications.

Note added. During the review process, we noted another study [81] suggesting FB may enhance catalytic performance.

DATA AVAILABILITY

The data that support the findings of this article are not publicly available. The data are available from the authors upon reasonable request.

[1] Z. Liu, F. Liu, and Y.-S. Wu, Exotic electronic states in the world of flat bands: From theory to material, Chin. Phys. B **23**, 077308 (2014).

[2] E. Tang, J.-W. Mei, and X.-G. Wen, High-temperature fractional quantum Hall states, Phys. Rev. Lett. **106**, 236802 (2011).

[3] H. Liu, G. Sethi, D. N. Sheng, Y. Zhou, J.-T. Sun, S. Meng, and F. Liu, High-temperature fractional quantum Hall state in the floquet kagome flat band, Phys. Rev. B **105**, L161108 (2022).

[4] K. Sun, Z. Gu, H. Katsura, and S. D. Sarma, Nearly flatbands with nontrivial topology, Phys. Rev. Lett. **106**, 236803 (2011).

[5] T. Neupert, L. Santos, C. Chamon, and C. Mudry, Fractional quantum Hall states at zero magnetic field, Phys. Rev. Lett. **106**, 236804 (2011).

[6] H. Park, J. Cai, E. Anderson, Y. Zhang, J. Zhu, X. Liu, C. Wang, W. Holtzmann, C. Hu, Z. Liu *et al.*, Observation of fractionally quantized anomalous Hall effect, Nature (London) **622**, 74 (2023).

[7] C. Repellin, The twisted material that splits the electron, Nature (London) **622**, 63 (2023).

[8] Y. Cao, V. Fatemi, A. Demir, S. Fang, S. L. Tomarken, J. Y. Luo, J. D. Sanchez-Yamagishi, K. Watanabe, T. Taniguchi, E. Kaxiras *et al.*, Correlated insulator behaviour at half-filling in magic-angle graphene superlattices, Nature (London) **556**, 80 (2018).

[9] Y. Cao, V. Fatemi, S. Fang, K. Watanabe, T. Taniguchi, E. Kaxiras, and P. Jarillo-Herrero, Unconventional superconductivity in magic-angle graphene superlattices, Nature (London) **556**, 43 (2018).

[10] M. Oh, K. P. Nuckolls, D. Wong, R. L. Lee, X. Liu, K. Watanabe, T. Taniguchi, and A. Yazdani, Evidence for unconventional superconductivity in twisted bilayer graphene, Nature (London) **600**, 240 (2021).

[11] C. Wu, D. Bergman, L. Balents, and S. D. Sarma, Flat bands and Wigner crystallization in the honeycomb optical lattice, Phys. Rev. Lett. **99**, 070401 (2007).

[12] B. Jaworowski, A. D. Güçlü, P. Kaczmarkiewicz, M. Kupczyński, P. Potasz, and A. Wójs, Wigner crystallization in topological flat bands, New J. Phys. **20**, 063023 (2018).

[13] Y. Chen, S. Xu, Y. Xie, C. Zhong, C. Wu, and S. B. Zhang, Ferromagnetism and Wigner crystallization in kagome graphene and related structures, Phys. Rev. B **98**, 035135 (2018).

[14] D. Jérome, T. M. Rice, and W. Kohn, Excitonic insulator, Phys. Rev. **158**, 462 (1967).

[15] G. Sethi, Y. Zhou, L. Zhu, L. Yang, and F. Liu, Flat-band-enabled triplet excitonic insulator in a diatomic kagome lattice, Phys. Rev. Lett. **126**, 196403 (2021).

[16] G. Sethi, M. Cuma, and F. Liu, Excitonic condensate in flat valence and conduction bands of opposite chirality, Phys. Rev. Lett. **130**, 186401 (2023).

[17] B. Hammer and J. K. Norskov, Why gold is the noblest of all the metals, Nature (London) **376**, 238 (1995).

[18] H. Liu, G. Sethi, S. Meng, and F. Liu, Orbital design of flat bands in non-line-graph lattices via line-graph wave functions, Phys. Rev. B **105**, 085128 (2022).

[19] X. Zhang, L. Wang, M. Li, W. Meng, Y. Liu, X. Dai, G. Liu, Y. Gu, J. Liu, and L. Kou, Topological surface state: Universal catalytic descriptor in topological catalysis, Mater. Today **67**, 23 (2023).

[20] J. Li, H. Ma, Q. Xie, S. Feng, S. Ullah, R. Li, J. Dong, D. Li, Y. Li, and X.-Q. Chen, Topological quantum catalyst: Dirac nodal line states and a potential electrocatalyst of hydrogen evolution in the TiSi family, Sci. China Mater. **61**, 23 (2018).

[21] Q. Yang, G. Li, K. Manna, F. Fan, C. Felser, and Y. Sun, Topological engineering of Pt-group-metal-based chiral crystals toward high-efficiency hydrogen evolution catalysts, Adv. Mater. **32**, 1908518 (2020).

[22] X. Kong, Z. Liu, Z. Geng, A. Zhang, Z. Guo, S. Cui, C. Xia, S. Tan, S. Zhou, Z. Wang *et al.*, Experimental demonstration of topological catalysis for CO_2 electroreduction, J. Am. Chem. Soc. **146**, 6536 (2024).

[23] Z. F. Wang, L. Chen, and F. Liu, Tuning topological edge states of Bi(111) bilayer film by edge adsorption, Nano Lett. **14**, 2879 (2014).

[24] Z. F. Wang, H. Zhang, D. Liu, C. Liu, C. Tang, C. Song, Y. Zhong, J. Peng, F. Li, C. Nie *et al.*, Topological edge states in a high-temperature superconductor FeSe/$SrTiO_3$(001) film, Nat. Mater. **15**, 968 (2016).

[25] A. Mielke, Ferromagnetic ground states for the Hubbard model on line graphs, J. Phys. A: Math. Gen. **24**, L73 (1991).

[26] A. Mielke, Ferromagnetism in the Hubbard model on line graphs and further considerations, J. Phys. A: Math. Gen. **24**, 3311 (1991).

[27] N. Regnault, Y. Xu, M.-R. Li, D.-S. Ma, M. Jovanovic, A. Yazdani, S. S. P. Parkin, C. Felser, L. M. Schoop, N. P. Ong *et al.*, Catalogue of flat-band stoichiometric materials, Nature (London) **603**, 824 (2022).

[28] A. Bhattacharya, I. Timokhin, R. Chatterjee, Q. Yang, and A. Mishchenko, Deep learning approach to genome of two-dimensional materials with flat electronic bands, npj Comput. Mater. **9**, 101 (2023).

[29] H. Liu, S. Meng, and F. Liu, Screening two-dimensional materials with topological flat bands, Phys. Rev. Mater. **5**, 084203 (2021).

[30] G. Sethi, B. Xia, D. Kim, H. Liu, X. Li, and F. Liu, Graph theorem for chiral exact flat bands at charge neutrality, Phys. Rev. B **109**, 035140 (2024).

[31] R. Bistritzer and A. H. MacDonald, Moiré bands in twisted double-layer graphene, Proc. Natl. Acad. Sci. USA **108**, 12233 (2011).

[32] Y. Yu, K. Zhang, H. Parks, M. Babar, S. Carr, I. M. Craig, M. Van Winkle, A. Lyssenko, T. Taniguchi, K. Watanabe *et al.*, Tunable angle-dependent electrochemistry at twisted bilayer graphene with moiré flat bands, Nat. Chem. **14**, 267 (2022).

[33] M. Pan, X. Zhang, Y. Zhou, P. Wang, Q. Bian, H. Liu, X. Wang, X. Li, A. Chen, X. Lei *et al.*, Growth of mesoscale ordered two-dimensional hydrogen-bond organic framework with the observation of flat band, Phys. Rev. Lett. **130**, 036203 (2023).

[34] A. Dhakshinamoorthy, Z. Li, and H. Garcia, Catalysis and photocatalysis by metal organic frameworks, Chem. Soc. Rev. **47**, 8134 (2018).

[35] Y. Shi, X. Zhang, H. Liu, J. Han, Z. Yang, L. Gu, and Z. Tang, Metalation of catechol-functionalized defective covalent organic frameworks for lewis acid catalysis, Small **16**, 2001998 (2020).

[36] M. Wang, M. Wang, H.-H. Lin, M. Ballabio, H. Zhong, M. Bonn, S. Zhou, T. Heine, E. Cánovas, R. Dong *et al.*, High-mobility semiconducting two-dimensional conjugated covalent organic frameworks with *p*-type doping, J. Am. Chem. Soc. **142**, 21622 (2020).

[37] R. Dong, P. Han, H. Arora, M. Ballabio, M. Karakus, Z. Zhang, C. Shekhar, P. Adler, P. S. Petkov, A. Erbe *et al.*, High-mobility band-like charge transport in a semiconducting two-dimensional metal–organic framework, Nat. Mater. **17**, 1027 (2018).

[38] S. Wan, F. Gándara, A. Asano, H. Furukawa, A. Saeki, S. K. Dey, L. Liao, M. W. Ambrogio, Y. Y. Botros, X. Duan *et al.*, Covalent organic frameworks with high charge carrier mobility, Chem. Mater. **23**, 4094 (2011).

[39] W. Jiang, X. Ni, and F. Liu, Exotic topological bands and quantum states in metal–organic and covalent–organic frameworks, Acc. Chem. Res. **54**, 416 (2021).

[40] E. H. Lieb, Two theorems on the Hubbard model, Phys. Rev. Lett. **62**, 1201 (1989).

[41] W. Jiang, S. Zhang, Z. Wang, F. Liu, and T. Low, Topological band engineering of lieb lattice in phthalocyanine-based metal–organic frameworks, Nano Lett. **20**, 1959 (2020).

[42] B. Pal, Nontrivial topological flat bands in a diamond-octagon lattice geometry, Phys. Rev. B **98**, 245116 (2018).

[43] M. Ezawa, Higher-order topological insulators and semimetals on the breathing kagome and pyrochlore lattices, Phys. Rev. Lett. **120**, 026801 (2018).

[44] K. Essafi, L. D. C. Jaubert, and M. Udagawa, Flat bands and dirac cones in breathing lattices, J. Phys.: Condens. Matter **29**, 315802 (2017).

[45] A. Mielke, Exact ground states for the hubbard model on the kagome lattice, J. Phys. A: Math. Gen. **25**, 4335 (1992).

[46] X. Ni, Y. Zhou, G. Sethi, and F. Liu, π-Orbital Yin–Yang kagome bands in anilato-based metal–organic frameworks, Phys. Chem. Chem. Phys. **22**, 25827 (2020).

[47] S. Zhang, M. Kang, H. Huang, W. Jiang, X. Ni, L. Kang, S. Zhang, H. Xu, Z. Liu, and F. Liu, Kagome bands disguised in a coloring-triangle lattice, Phys. Rev. B **99**, 100404(R) (2019).

[48] Y. Gao, Y.-Y. Zhang, J.-T. Sun, L. Zhang, S. Zhang, and S. Du, Quantum anomalous Hall effect in two-dimensional cudicyanobenzene coloring-triangle lattice, Nano Res. **13**, 1571 (2020).

[49] M. Chen and S. Wan, The quantum anomalous Hall effect on a star lattice with spin–orbit coupling and an exchange field, J. Phys.: Condens. Matter **24**, 325502 (2012).

[50] Y. Zhou, G. Sethi, C. Zhang, X. Ni, and F. Liu, Giant intrinsic circular dichroism of enantiomorphic flat chern bands and flatband devices, Phys. Rev. B **102**, 125115 (2020).

[51] T. Hu, T. Zhang, H. Mu, and Z. Wang, Intrinsic second-order topological insulator in two-dimensional covalent organic frameworks, J. Phys. Chem. Lett. **13**, 10905 (2022).

[52] Y. Zhou, G. Sethi, H. Liu, Z. Wang, and F. Liu, Excited quantum anomalous and spin Hall effect: Dissociation of flat-bands-enabled excitonic insulator state, Nanotechnology **33**, 415001 (2022).

[53] T. Hu, W. Zhong, T. Zhang, W. Wang, and Z. F. Wang, Identifying topological corner states in two-dimensional metal-organic frameworks, Nat. Commun. **14**, 7092 (2023).

[54] M. Ko, L. Mendecki, and K. A. Mirica, Conductive two-dimensional metal–organic frameworks as multifunctional materials, Chem. Commun. **54**, 7873 (2018).

[55] G. Bian, J. Yin, and J. Zhu, Recent advances on conductive 2D covalent organic frameworks, Small **17**, 2006043 (2021).

[56] J.-Y. You, B. Gu, and G. Su, Flat band and hole-induced ferromagnetism in a novel carbon monolayer, Sci. Rep. **9**, 20116 (2019).

[57] D.-Y. Li, Y. Wang, X.-Y. Hou, Y.-T. Ren, L.-X. Kang, F.-H. Xue, Y.-C. Zhu, J.-W. Liu, M. Liu, X.-Q. Shi *et al.*, On-surface synthesis of [3]radialenes via [1+1+1] cycloaddition, Angew. Chem. Int. Ed. **61**, e202117714 (2022).

[58] C.-K. Lyu, Y.-F. Gao, Z.-A. Gao, S.-Y. Mo, M.-Q. Hua, E. Li, S.-Q. Fu, J.-Y. Chen, P.-N. Liu, L. Huang *et al.*, Synthesis of single-layer two-dimensional metal–organic frameworks $M_3(HAT)_2$ (M = Ni, Fe, Co, HAT = 1,4,5,8,9,12-Hexaazatriphenylene) using an on-surface reaction, Angew. Chem. Int. Ed. **61**, e202204528 (2022).

[59] G. Kresse and J. Hafner, *Ab initio* molecular dynamics for liquid metals, Phys. Rev. B **47**, 558 (1993).

[60] G. Kresse and J. Furthmüller, Efficiency of *ab-initio* total energy calculations for metals and semiconductors using a plane-wave basis set, Comput. Mater. Sci. **6**, 15 (1996).

[61] J. P. Perdew, K. Burke, and M. Ernzerhof, Generalized gradient approximation made simple, Phys. Rev. Lett. **77**, 3865 (1996).

[62] S. Grimme, J. Antony, S. Ehrlich, and H. Krieg, A consistent and accurate *ab initio* parametrization of density functional dispersion correction (DFT-D) for the 94 Elements H-Pu, J. Chem. Phys. **132**, 154104 (2010).

[63] M. Dion, H. Rydberg, E. Schröder, D. C. Langreth, and B. I. Lundqvist, van der waals density functional for general geometries, Phys. Rev. Lett. **92**, 246401 (2004).

[64] H. J. Monkhorst and J. D. Pack, Special points for brillouin-zone integrations, Phys. Rev. B **13**, 5188 (1976).

[65] J. K. Nørskov, T. Bligaard, A. Logadottir, J. R. Kitchin, J. G. Chen, S. Pandelov, and U. Stimming, Trends in the exchange current for hydrogen evolution, J. Electrochem. Soc. **152**, J23 (2005).

[66] C. G. Morales-Guio, L.-A. Stern, and X. Hu, Nanostructured hydrotreating catalysts for electrochemical hydrogen evolution, Chem. Soc. Rev. **43**, 6555 (2014).

[67] Y. Song, W.-H. Dong, K.-R. Hao, S. Du, and L. Zhang, Designing topological and correlated 2D magnetic states via superatomic lattice constructions of zirconium dichloride, Nano Res. **16**, 13509 (2023).

[68] See Supplemental Material at http://link.aps.org/supplemental/10.1103/56zz-7kwp for phonon spectrum, *ab initio* molecular dynamics simulations, and electronic properties of 3R-*X* COFs and HAT-*M* MOFs.

[69] L. Fu and C. L. Kane, Topological insulators with inversion symmetry, Phys. Rev. B **76**, 045302 (2007).

[70] Y. Zheng, Y. Jiao, Y. Zhu, L. H. Li, Y. Han, Y. Chen, A. Du, M. Jaroniec, and S. Z. Qiao, Hydrogen evolution by a metal-free electrocatalyst, Nat. Commun. **5**, 3783 (2014).

[71] B. Hinnemann, P. G. Moses, J. Bonde, K. P. Jørgensen, J. H. Nielsen, S. Horch, I. Chorkendorff, and J. K. Nørskov, Biomimetic hydrogen evolution: MoS_2 nanoparticles as catalyst for hydrogen evolution, J. Am. Chem. Soc. **127**, 5308 (2005).

[72] D. Cao, H. Xu, H. Li, C. Feng, J. Zeng, and D. Cheng, Volcano-type relationship between oxidation states and catalytic activity of single-atom catalysts towards hydrogen evolution, Nat. Commun. **13**, 5843 (2022).

[73] T. Zhang, Z. Jiang, and A. M. Rappe, Hydrogenation of covalent organic framework induces conjugated π bonds and electronic

topological transition to enhance hydrogen evolution catalysis, J. Am. Chem. Soc. **146**, 15488 (2024).

[74] S. Trasatti, Work function, electronegativity, and electrochemical behaviour of metals: III. Electrolytic hydrogen evolution in acid solutions, J. Electroanal. Chem. Interfacial Electrochem. **39**, 163 (1972).

[75] J. Perez, E. R. Gonzalez, and H. M. Villullas, Hydrogen evolution reaction on gold single-crystal electrodes in acid solutions, J. Phys. Chem. B **102**, 10931 (1998).

[76] J. O'M. Bockris and A. K. N. Reddy, *Modern Electrochemistry* (Plenum Press, New York, 1970), Vol. 2.

[77] D. Eberhardt, E. Santos, and W. Schmickler, Hydrogen evolution on silver single crystal electrodes—first results, J. Electroanal. Chem. **461**, 76 (1999).

[78] O. Savadogo and D. L. Piron, New hydrogen cathodes in acid medium: Case of nickel electrodeposited with Heteropolyacids (HPAs), Int. J. Hydrogen Energy **15**, 715 (1990).

[79] N. M. Markovic and P. N. Ross, in *Interfacial Electrochemistry*, edited by A. Wieckowski (Marcel Dekker, New York, 1999).

[80] X. Tan, H. A. Tahini, and S. C. Smith, *p*-Doped graphene/graphitic carbon nitride hybrid electrocatalysts: Unraveling charge transfer mechanisms for enhanced hydrogen evolution reaction performance, ACS Catal. **6**, 7071 (2016).

[81] Y. Huang, Y. Chen, S. Zhang, Z. Zhang, and P. Cui, High-density natural active sites for efficient nitrogen reduction on kagome surfaces promoted by flat bands, npj Comput. Mater. **11**, 154 (2025).